ISSN 1674-1056
http://cpb.iphy.ac.cn
http://iopscience.iop.org/cpb
中国物理 B
Chinese Physics
中国物理 Chinese Physics B

Mn-based permanent magnets

Jinbo Yang(杨金波), Wenyun Yang(杨文云), Zhuyin Shao(邵珠印), Dong Liang(梁栋), Hui Zhao(赵辉), Yuanhua Xia(夏元华), Yunbo Yang(杨云波)

Citation: Chin. Phys. B . 2018, 27(11): 117503. **doi:** 10.1088/1674-1056/27/11/117503

Journal homepage: http://cpb.iphy.ac.cn; http://iopscience.iop.org/cpb

What follows is a list of articles you may be interested in

Structural, Mössbauer spectroscopy, magnetic properties, and thermal measurements of $Y_{3-x}Dy_xFe_5O_{12}$

Mahdi Lataifeh, Qassem I Mohaidat, Sami H Mahmood, Ibrahim Bsoul, Mufeed Awawdeh, Ibrahim Abu-Aljarayesh, Mu'ath Altheeba

Chin. Phys. B . 2018, 27(10): 107501. **doi:** 10.1088/1674-1056/27/10/107501

Effects of dipolar interactions on magnetic properties of Co nanowire arrays

Hong-Jian Li(李洪健), MingYue(岳明), Qiong Wu(吴琼), Yi Peng(彭懿), Yu-Qing Li(李玉卿), Wei-Qiang Liu(刘卫强), Dong-Tao Zhang(张东涛), Jiu-Xing Zhang(张久兴)

Chin. Phys. B . 2017, 26(11): 117503. **doi:** 10.1088/1674-1056/26/11/117503

Magnetic properties of Sn-substituted Ni–Zn ferrites synthesized from nano-sized powders of NiO, ZnO, Fe_2O_3, and SnO_2

M A Ali, M M Uddin, M N I Khan, F U Z Chowdhury, S M Hoque, S I Liba

Chin. Phys. B . 2017, 26(7): 077501. **doi:** 10.1088/1674-1056/26/7/077501

Low temperature ferromagnetic properties of CdS and CdTe thin films

Hafiz Tariq Masood, Zahir Muhammad, Muhammad Habib, Dong-Ming Wang(王东明), De-Liang Wang(王德亮)

Chin. Phys. B . 2017, 26(6): 067503. **doi:** 10.1088/1674-1056/26/6/067503

Structural and magnetic properties of turmeric functionalized $CoFe_2O_4$ nanocomposite powder

E Mehran, S Farjami Shayesteh, M Sheykhan

Chin. Phys. B . 2016, 25(10): 107504. **doi:** 10.1088/1674-1056/25/10/107504

TOPICAL REVIEW — Magnetism, magnetic materials, and interdisciplinary research

Mn-based permanent magnets*

Jinbo Yang(杨金波)[1,2,3,†], Wenyun Yang(杨文云)[1,2,3], Zhuyin Shao(邵珠印)[1,2,3], Dong Liang(梁栋)[1,2,3], Hui Zhao(赵辉)[1,2,3], Yuanhua Xia(夏元华)[4], and Yunbo Yang(杨云波)[1]

[1] State Key Laboratory for Mesoscopic Physics, School of Physics, Peking University, Beijing 100871, China
[2] Collaborative Innovation Center of Quantum Matter, Beijing 100871, China
[3] Beijing Key Laboratory for Magnetoelectric Materials and Devices, Beijing 100871, China
[4] Institutes of Nuclear Physics and Chemistry, China Academy of Engineering Physics, Mianyang 621999, China

(Received 23 September 2018; published online 25 October 2018)

Mn-based intermetallic compounds have attracted much attention due to their fascinating structural and physical properties, especially their interesting hard magnetic properties. In this paper, we have summarized the magnetic and structural properties of Mn-based intermetallic compounds (MnX, where X = Al, Bi, and Ga). Various methods for synthesizing single phases of MnAl, MnBi, and Mn$_x$Ga were developed in our lab. A very high saturation magnetization of 125 emu/g, coercivity of 5 kOe, and maximum energy product $(BH)_{\max}$ of 3.1 MG·Oe were achieved at room temperature for the pure τ-Mn–Al magnetic phase without carbon doping and the extrusion process. Low temperature phase (LTP) MnBi with a purity above 95 wt.% can be synthesized. An abnormal temperature coefficient of the coercivity was observed for the LTP MnBi magnet. Its coercivity increased with temperature from 100 K to 540 K, reached a maximum of 2.5 T at about 540 K, and then decreased slowly to 1.8 T at 610 K. The positive temperature coefficient of the coercivity is related to the evolution of the structure and magnetocrystalline anisotropy field of the LTP MnBi phase with temperature. The LTP MnBi bonded magnets show maximum energy products $(BH)_{\max}$ of 8.9 MG·Oe (70 kJ/m^3) and 5.0 MG·Oe (40 kJ/m^3) at room temperature and 400 K, respectively. Ferrimagnetic Mn$_x$Ga phases with L1$_0$ structures ($x < 2.0$) and D0$_{22}$ structures ($x > 2.0$) were obtained. All of the above structures can be described by a D0$_{22}$ supercell model in which 2a-Ga and 2b-Mn are simultaneously substituted. The tetragonal D0$_{22}$ phases of the Mn$_x$Ga show high coercivities ranging from 7.2 kOe for low Mn content $x = 1.8$ to 18.2 kOe for high Mn content $x = 3$ at room temperature. The Mn$_{1.2}$Ga sample exhibits a room temperature magnetization value of 80 emu/g. The hard magnetic properties of coercivity $_{\mathrm{i}}H_{\mathrm{c}} = 3.5$ kOe, remanence $M_{\mathrm{r}} = 43.6$ emu/g, and $(BH)_{\max} = 2.5$ MG·Oe were obtained at room temperature. Based on the above studies, we believe that Mn-based magnetic materials could be promising candidates for rare earth free permanent magnets exhibiting a high Curie temperature, high magnetocrystalline anisotropy, and very high coercivity.

Keywords: permanent magnetic materials, magnetic properties, manganese alloys, magnetic structure, coercivity, magnetization, neutron diffraction

PACS: 75.50.Ww, 75.60.–d, 75.75.–c, 61.05.F– **DOI:** 10.1088/1674-1056/27/11/117503

1. Introduction

To date, studies of rare-earth-transition metal intermetallic compounds have paved the way for the production of high performance permanent magnets that significantly impact the green energy applications.[1–7] The present high performance rare earth permanent magnets contain the transition metals Fe and Co, which are capable of carrying a large magnetic moment in metallic compounds. Co (with a typical moment of 1.6 μ_{B}) is used in $CaCu_5$-type structures with Sm to form SmCo binary compounds (1:5, 2:17, 1:7), while Fe (with about 2.0 μ_{B}) is the principal constituent in the $R_2Fe_{14}B$ (2:14:1), R(Fe, M)$_{12}$N$_x$ (R = Pr, Nd, M = Ti, V, Mo, ...) (1:12), and $Sm_2Fe_{17}N_x$ (2:17) families of compounds. These compounds are characterized by uniaxial hexagonal or tetragonal crystal structures that are the basis for large magnetocrystalline anisotropies. However, rare earth elements, such as Pr, Nd, and Dy, are relatively scare and strategically undesirable, which presents a great opportunity for the study of low-cost and environmentally sustainable magnetic metal alloys without rare earth elements or noble metals.[7,8] Mn is another inexpensive 3d metal that can support high magnetic moments but is not presently the major constituent of permanent magnets. However, most of the Mn-based alloys normally exhibit antiferromagnetic behavior and are not well investigated. There are a few compounds containing Mn that exhibit ferromagnetic exchange interactions, including binary alloys Mn–Al, Mn–Ga, Mn–Bi, Mn–Ge, Mn–As, Mn–Si, and Mn-based Heusler alloys. Among them, the ferromagnetic τ-phase MnAl phase (L1$_0$), tetragonal Mn$_x$Ga phase, and low temperature phase (LTP) MnBi have recently received a considerable amount of attention because of their high magnetic moments, high magnetic crystalline anisotropy constants, and high Curie

*Project supported by the National Natural Science Foundation of China (Grant Nos. 51731001, 11805006, 51371009, 11504348, and 11675006) and the National Key Research and Development Program of China (Grant Nos. 2016YFB0700901, 2017YFA0401502, and 2017YFA0206303).

†Corresponding author. E-mail: jbyang@pku.edu.cn

© 2018 Chinese Physical Society and IOP Publishing Ltd

temperatures. They therefore exhibit a potential use as permanent magnets.[9–33]

2. Mn–Al hard magnetic phase

In 1958, Kono first discovered the presence of a ferromagnetic τ-phase in Mn–Al alloys,[9] and Koch used the pulverization method to obtain MnAl permanent magnetic alloys with a coercivity of 0.6 T.[10] The τ-phase Mn–Al is the only ferromagnetic phase of Mn–Al alloys and was considered as one of the promising candidates for rare earth free magnets owing to its high magnetic moment (2.4 μ_B/f.u.) and Curie temperature (650 K), large magnetocrystalline anisotropy constant (1.7 MJ/m^3), low cost, and good machinability.[11–16] The ferromagnetic τ phase exists in compounds with an Mn composition that varies from 51 at.% to 59 at.%, with an ordered body-centered tetragonal ($L1_0$) structure.[11] The Mn atoms occupy the 1*a* (0, 0, 0) site and couple ferromagnetically with the Al atoms, and any Mn atoms in excess of the equiatomicity enter the 1*d* (1/2, 1/2, 1/2) site coupled antiferromagnetically with Mn at 1*a* (0, 0, 0) sites.[12–14] As the τ phase is metastable, various heat treatments have been used to obtain and preserve the τ-phase.[15–27] More structurally stable τ-phase MnAl alloys were fabricated by adding a small amount of carbon into the MnAl alloy and possess improved mechanical properties, including a better machinability[11,14,15,28–30] and Curie temperatures and anisotropy fields that are lower than those of undoped alloys.[11,15] The pure τ-phase MnAl can be prepared by annealing the arc-melting ingots at 1050 °C for two days and allowing them to cool in air.[24] The Mn–Al alloy with a coercivity value of up to 5 kOe was obtained by Lu *et al.* using melt spinning and milling.[25] The τ-phase MnAl was produced by Chaturvedi *et al.* via gas atomization.[23] Fang *et al.* directly obtained phase MnAl from casting $Mn_{0.54}Al_{0.46}$ using the drop synthesis method.[26] However, the τ-phase tends to decompose or transform into nonmagnetic phases (i.e., the γ_2 and β phases). The τ-phase Mn–Al alloys prepared in previous studies consist of equilibrium phases, such as γ_2 and β phases, which depend on the preparation method and annealing temperature or time. It is worth noting that the coercivity, saturation magnetization M_s, and maximum energy product $(BH)_{max}$ of Mn–Al magnets are still very low compared to the theoretical values.[23–27]

To exploit the potential of the MnAl τ-phase as a hard magnetic material, we have used different methods to obtain the pure τ-phase and investigated their magnetic properties.[18,19,24] It was found that the amount of τ-MnAl in the final product strongly depends on the starting content of the Mn in the alloys and the preparation methods. Several different methods, including (i) melt spinning,[18] (ii) strip casting,[19] (iii) conventional arc melting,[24] were applied to prepare the τ-MnAl phase. Figure 1 shows the typical x-ray diffraction (XRD) patterns of $Mn_{54}Al_{46}$ alloys prepared using arc melting methods. As shown in Fig. 1(a), a ferromagnetic τ phase with a small amount of $\beta + \gamma_2$-phases was observed in the as-prepared arc-melting ingots. After heat treatment at 1050 °C for two days and a slow cooling down to room temperature, the $\beta + \gamma_2$-phases disappeared and an almost pure τ-phase was observed, as shown in Fig. 1(b). This is consistent with the observation that the high temperature ε-phase (h.c.p) first forms at 1050 °C , and then transforms to the ferromagnetic τ-phase following sufficient cooling.[30] According to the Mn–Al phase diagram,[10] the ferromagnetic Mn–Al phase is able to form in compounds with Mn atomic contents of 51% to 59%. To determine the specific τ-MnAl phase region, we tried to prepare $Mn_{55-x}Al_{45+x}$ ($x = 0, 1, 2, 3$) alloys using the the same method. The XRD patterns shown in Fig. 2 suggest that only $Mn_{54}Al_{46}$ could easily form the single τ-phase MnAl. The equilibrium phase of the β-phase appears in the Mn rich $Mn_{55}Al_{45}$ alloy, while the equilibrium $\beta + \gamma_2$-phases occur in the more Al-rich $Mn_{53}Al_{47}$ and $Mn_{52}Al_{48}$ alloys. As the composition $Mn_{54}Al_{46}$ is more suitable for the formation of single τ phase MnAl, an atomic ratio of 54:46 for Mn:Al is chosen as the starting composition to produce the high purity ferromagnetic τ-phase with high performance.

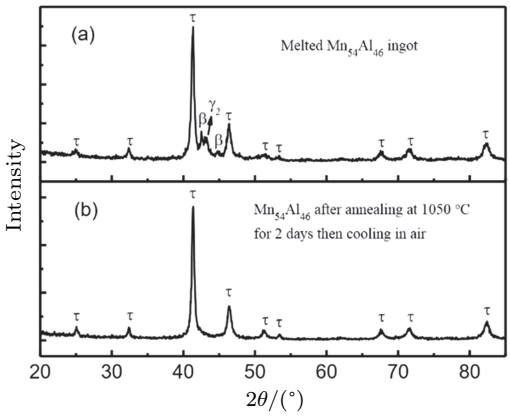


Fig. 1. XRD patterns of $Mn_{54}Al_{46}$ (a) as a prepared arc-melting ingot and (b) after annealing at 1050 °C for two days and cooling to room temperature.

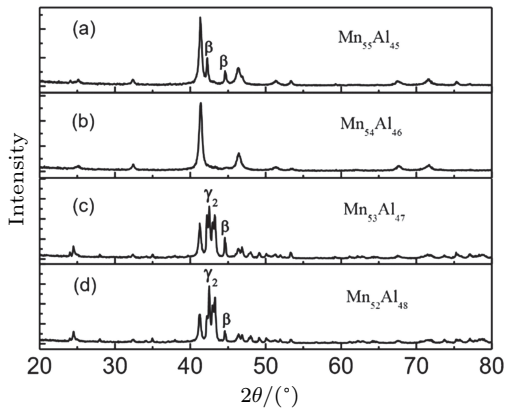


Fig. 2. XRD patterns of $Mn_{55-x}Al_{45+x}$ ingots annealed at 1050 °C for two days and cooled to room temperature: (a) $x = 0$, (b) $x = 1$, (c) $x = 2$, (d) $x = 3$.

As for the carbon doped MnAl alloys, alloys with compositions of $Mn_{54-x}Al_{46}C_x$ ($x = 0$, 1, 2, 3) were prepared by method (iii). The XRD patterns of $Mn_{54-x}Al_{46}C_x$ ($x = 0$, 1, 2, 3) ingots after annealing and then cooling in air are shown in Fig. 3, all of which form the pure τ phase. In contrast to our results, Zeng *et al.*[30] showed that the $Mn_{52.5}Al_{46}C_{1.5}$ alloy could not form a pure phase by conventional melting, and this difference may be due to differences in composition and heat treatment process. The XRD peaks of the $Mn_{54-x}Al_{46}C_x$ ($x = 1$, 2, 3) are narrower and more intense than those of the carbonfree samples. This reveals that the addition of C contributes to the formation of the τ phase by releasing the internal stress of the sample. The correlated differential thermal analysis also shows that C-doped MnAl is easier to form and has a better stability.

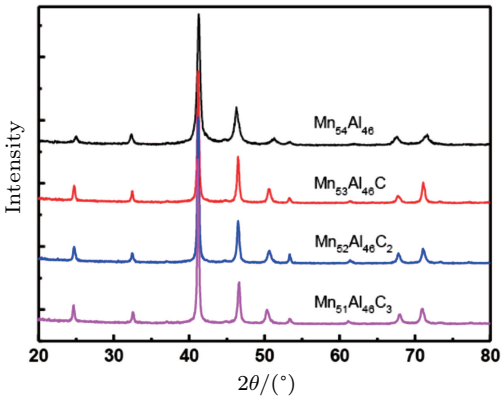


Fig. 3. (color online) XRD patterns of $Mn_{54-x}Al_{46}C_x$ ($x = 0$, 1, 2, 3) ingots annealed at 1050 °C for two days and then cooled to room temperature.

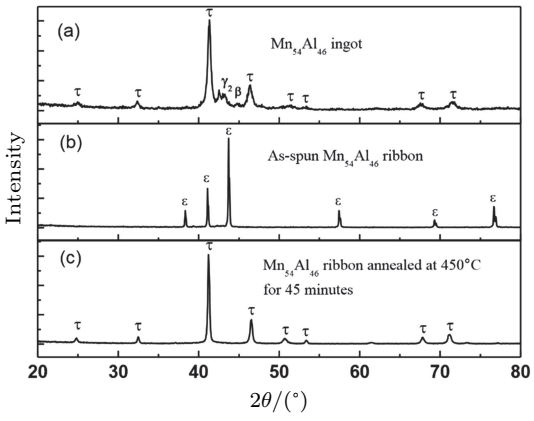


Fig. 4. XRD patterns of the $Mn_{54}Al_{46}$ alloys prepared with method (ii) (melt spinning speed is 30 m/s) at different steps (a)–(c).

Figure 4 shows the XRD patterns of the $Mn_{54}Al_{46}$ alloys prepared with method (i) at different steps. The main phase in the resulting $Mn_{54}Al_{46}$ ingot is the τ-MnAl phase, but it contains a small amount of the equilibrium $\beta + \gamma_2$ phases (Fig. 4(a)). $Mn_{54}Al_{46}$ completely retains the high-temperature nonmagnetic ε phase (Fig. 4(b)) in the ribbon samples obtained at a melt spinning speed of 30 m/s. The samples were annealed at 450 °C for 45 min and then fully transformed into the τ-MnAl magnetic phase (Fig. 4(c)). The XRD peaks of the τ-MnAl magnetic phase are sharper than those of the samples prepared with method (iii). The difference in the width of the diffraction peak reveals that there should be different microstructures in the samples. The pure $Mn_{54-x}Al_{46}C_x$ ($x = 1$, 2, 3) τ-magnetic phase can also be directly obtained by annealing the corresponding ribbons at 450 °C for 45 min (data not shown here).

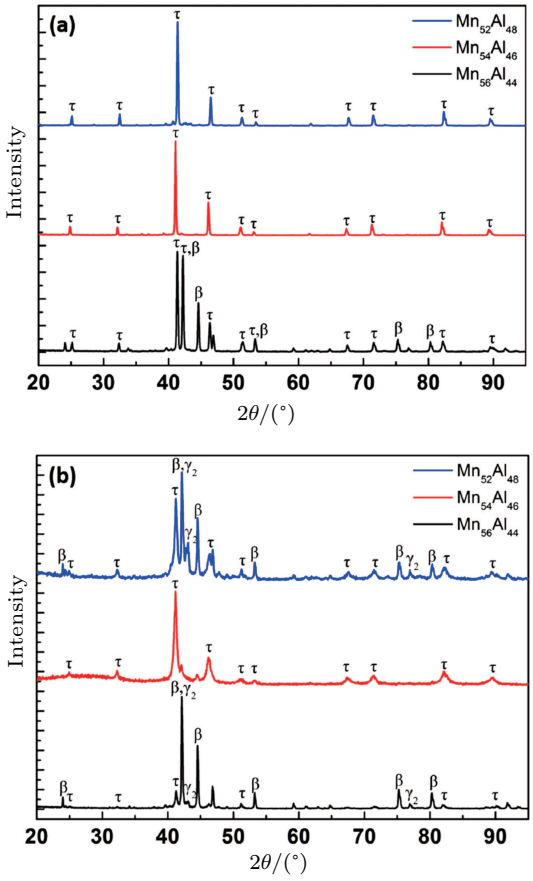


Fig. 5. (color online) XRD of free surfaces of MnAl strip samples and powder samples with different compositions: (a) $Mn_{52}Al_{48}$, $Mn_{54}Al_{46}$, and $Mn_{56}Al_{44}$ strip samples; (b) $Mn_{52}Al_{48}$, $Mn_{54}Al_{46}$, and $Mn_{56}Al_{44}$ powder samples.[19]

The strip casting technique has been employed to produce large amounts of strips of $Mn_{52}Al_{48}$, $Mn_{54}Al_{46}$, and $Mn_{56}Al_{44}$ alloys.[19] The as-prepared strips were milled into powders to study their structures and magnetic properties. Figure 5 shows the XRD patterns of the as-prepared MnAl strips and their powder samples. It is obvious that only the τ-phase was detected on the free-surfaces of the $Mn_{52}Al_{48}$ and $Mn_{54}Al_{46}$ strips (Fig. 5(a)), while both the β- and γ_2-phases appeared in the $Mn_{56}Al_{44}$ strip. After the strips were milled into powders, many more β-phases and γ_2-phases were detected, as shown in the XRD patterns of $Mn_{52}Al_{48}$ and $Mn_{56}Al_{44}$ powder samples (see Fig. 5(b)). This can be attributed to two effects: (A) the decomposition of the metastable τ-phase into β- and γ_2-phases because of the high defect density introduced in the grinding process.[26,27,31] Similarly, the β-phase and γ_2-phase content

increases with an increase in milling time for the $Mn_{54}Al_{46}$ powder samples with different milling times (data not shown here). (B) The cooling rate of the surface and that of the inside of the strip for strip samples are different, which may lead to a lack of complete uniformity in the phase compositions of the surfaces and insides of the strips. Generally, during the grinding process, the increase in strain and the decrease in grain size induce broadening of the diffraction peaks of $Mn_{54}Al_{46}$ powders as shown in Fig. 5(b). The XRD data of $Mn_{54}Al_{46}$ powders indicates that the nearly pure MnAl τ-phase could be observed together with tiny amounts of the β-phase and γ_2-phase, meaning that a high purity τ-phase can be achieved by choosing the starting composition of the $Mn_{54}Al_{46}$ alloy.

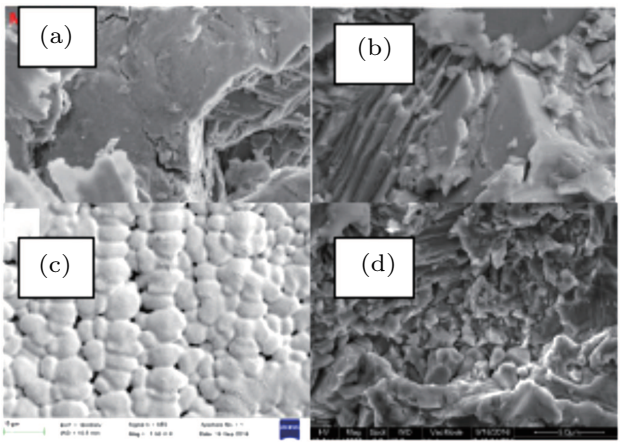


Fig. 6. SEM images of the microstructures of τ-MnAl alloys prepared by different methods: (a) and (b) for method (iii), (c) for method (i), and (d) is the ground powders from (c).

Figure 6 shows the SEM images of the microstructures for the τ-MnAl alloys prepared by different methods. For the MnAl alloy prepared using method (iii) (Fig. 6(a)), the microstructure consists of many twin related substructures, which are related to the ε–τ phase transformation processes.[17,31] The transformation from the ε to τ phase occurs via a compositionally invariant, diffusion nucleation, and growth process.[31,32] The long range stresses associated with the different lamellae result in the formation of the twin bands that can be seen in Fig. 6(b). Compared to those of method (iii), the grains of the $Mn_{54}Al_{46}$ strip sample prepared by method (i) show uniform size distribution and relatively completed separation (Fig. 6(c)). The uniform size distribution with relatively complete separation in $Mn_{54}Al_{46}$ alloys is helpful for the phase transformation that occurs during the strip casting process. As shown in Fig. 6(d), the grains of the $Mn_{54}Al_{46}$ powder sample show a fine layer-like structure that results from a martensitic shear reaction. This layer-like structure may preserve a large strain during the grinding process, leading to a broadening of the peak in the XRD patterns.

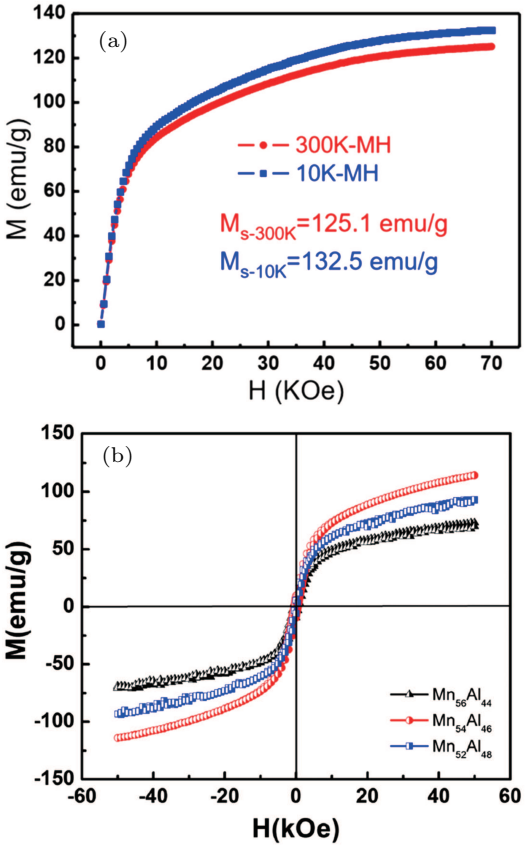


Fig. 7. (color online) *M*-*H* curves for τ-$Mn_{54}Al_{46}$ alloys prepared by (a) method (iii) and (b) method (i).[19]

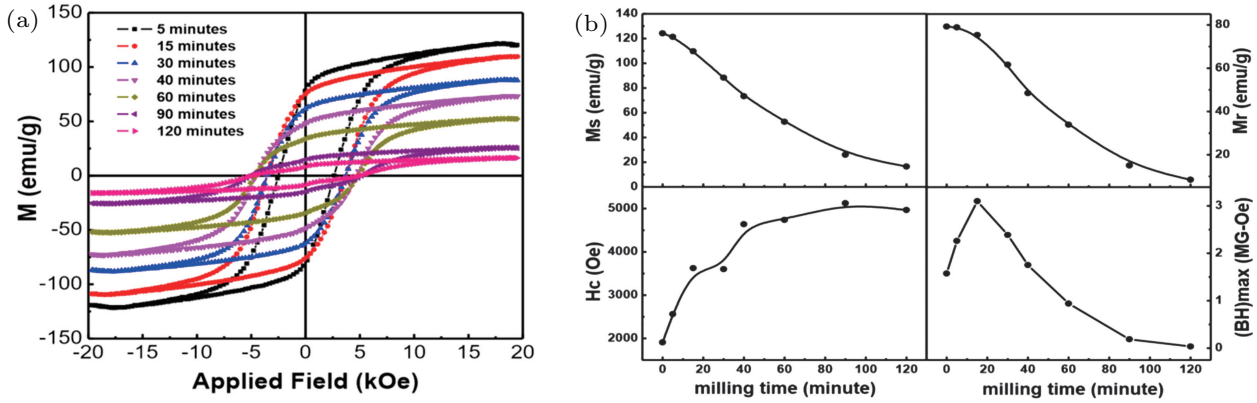


Fig. 8. (color online) (a) Hysteresis loops and (b) magnetic properties of $Mn_{54}Al_{46}$ powders prepared by method (iii) and milled for different durations.

Figure 7 shows the M–H curve for τ-$Mn_{54}Al_{46}$ alloys prepared with methods (i) and (iii). The room temperature magnetization of 114 emu/g and 125 emu/g can be obtained at a magnetic field of 5 T for methods (i) and (iii), respectively. These values are higher than those of the previous reports.[16,20,30] The magnetization is critical to obtaining a high maximum energy product.

To further improve the magnetic properties of the alloys, the alloys were mechanically milled to fine powders for different durations. The fine powders were fixed into an epoxy resin and subjected to a magnetic field of about 1.0 T to form magnetically aligned samples of cylindrical shape. The hysteresis loops of the powders from the annealed samples with different grinding durations are shown in Fig. 8. It can be seen from Fig. 8(b) that coercivity increases quickly with grinding duration and reaches its maximum of 5 kOe at about 90 min. The increase in coercivity is partly due to grain refinement. In addition, the increase in grain boundary and lattice defects caused by grinding also increases the coercivity of the pinning mechanism. The magnetization decreases with milling time, which is due to the decomposition and Mn–Al disorder effects in the grinding process.[12,13,31] This can be observed from the change in the peaks intensity with milling time (see Fig. 9). As the [100] and [001] peaks are related to the Mn–Al site ordering, the disappearance of these two peaks is related to the Mn–Al site disorder. As the atomic ratio of Mn is over 50%, extra Mn will go to the Al sites 1d (1/2, 1/2, 1/2), which will couple with the Mn on site 1a (0, 0, 0) in an antiparallel manner, and reduce the total magnetization. Thus, this suggests that it is critical to prevent the disorder effect in MnAl alloys. The best magnetic properties of coercivity ${}_{\mathrm{i}}H_{\mathrm{c}} = 3.7$ kOe, remanence $M_{\mathrm{r}} = 72.6$ emu/g, and $(BH)_{\max} = 3.1$ MG·Oe at RT can be obtained for the sample that was milled for 15 min. Magnetic properties of coercivity ${}_{\mathrm{i}}H_{\mathrm{c}} = 6.0$ kOe, remanence $M_{\mathrm{r}} = 79$ emu/g, and maximum energy product $(BH)_{\max} = 4.9$ MG·Oe were achieved at 10 K.

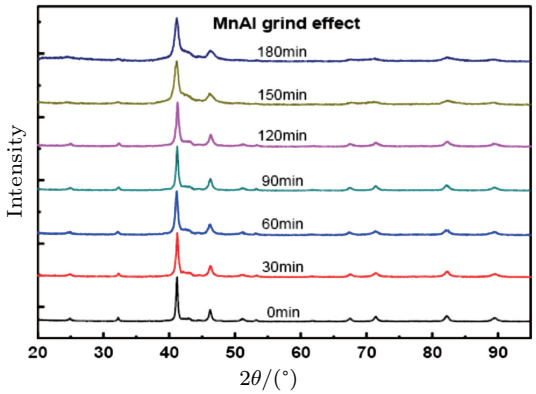


Fig. 9. (color online) XRD patterns of MnAl powders prepared by method (iii) and milled for different durations.

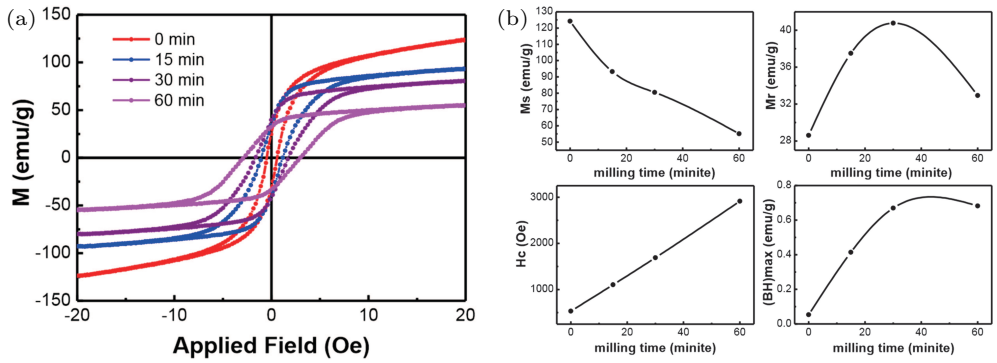


Fig. 10. (color online) (a) Hysteresis loops and (b) magnetic properties of $Mn_{51}Al_{46}C_3$ powders prepared by method (iii) and milled for different durations.

Similar to that of $Mn_{54}Al_{46}$, the saturation magnetization of $Mn_{51}Al_{46}C_3$ decreases with an increase in milling time, and decreases from 124.2 emu/g to 55.1 emu/g after 60 min, while the coercive force increases linearly from 531.6 Oe to 2931 Oe (Fig. 10). As the initial coercive force is too small, the residual magnetization increases with increasing coercive force, reaches its maximum value after 30 min of grinding, and then begins to decrease. The best permanent magnetic properties are obtained after grinding for 60 min. The magnetic properties are coercivity ${}_{\mathrm{i}}H_{\mathrm{c}} = 2.93$ kOe and residual magnetization $M_{\mathrm{r}} = 32.9$ emu/g. The maximum energy product of $Mn_{51}Al_{46}C_3$ is much smaller than that of $Mn_{54}Al_{46}$.

The saturation magnetization of MnAl(C) decreases significantly with milling time, which is not due to the phase transition induced by grinding, as no new diffraction peaks are found in the XRD and neutron diffraction (ND) patterns (data not shown here). The reason for the decrease in the saturation magnetization may include: (A) The crystal interface is increased after grain refinement. In 1966, Zijlstra *et al.* observed the antiferromagnetic coupling of the lattice defect boundary using a Lorentz microscope.[32] (B) The XRD background growth indicates the presence of amorphous components, which may also reduce the saturation magnetization, because amorphous components generally do not show strong ferromagnetism. The saturation magnetization decreases from 124.1 emu/g to 16.5 emu/g, which is reduced by 86.7% with an increase in milling time. The above two reasons are not sufficient to explain the decrease in the saturation magnetization

with milling time. Another important reason for the decrease in saturation magnetization is that the milling leads to an increase in the disorder of the atomic occupancy in the MnAl(C) magnetic phase so that more Mn atoms appear in the antiferromagnetic coupling state.[13,14]

The coercivities of all as-prepared strip Mn–Al samples were less than 1 kOe. The strips were further milled into powders with a particle size of less than 0.1 mm to study their magnetic properties. The coercivities of the powder samples showed a value of 2.8 kOe, indicating a significant increase, when compared with those of the as-prepared strip samples. The measured magnetizations M_{5T} for $Mn_{54}Al_{46}$ and $Mn_{56}Al_{44}$ powder samples were 63.9 emu/g. They are lower than those of the strip samples due to the decomposition and Mn–Al disorder effect in the grinding process. Besides, the amorphous-like phase, which can be detected by an increase in the XRD background, also makes a contribution.

We also successfully prepared the Ga-substituted τ-phase $Mn_{54.5}Al_{45.5-x}Ga_x$ ($x = 0.0$, 15.0, 25.0, 35.0, 45.5) with $L1_0$ structure by meltspinning and subsequent annealing.[18] The site-specific ordering and magnetic structure were determined by XRD and ND (see Figs. 11 and 12). In particular, we found that Al and Ga atoms both occupy the 1*a* (0, 0, 0) and 1*d* (1/2, 1/2, 1/2) sites, and show a preference for occupying the 1*d* site. With an increase in Ga content *x*, the lattice parameter *a* slightly decreased, while *c* abnormally increased, which is due to the fact that the Ga atom located at the 1*d* sites is larger than that of Al. The mass magnetization decreased from 134 emu/g to 91 emu/g at 5 K as *x* increased from 0.0 to 45.5 owing to higher density of the alloys with Ga. The Curie temperature decreased almost linearly from 644 K for $Mn_{54.5}Al_{45.5}$ to 578 K for $Mn_{54.5}Ga_{45.5}$ owing to the decrease in the ferromagnetic Mn–Mn interaction in the *a*–*b* plane. A coercivity ($_iH_c$) value of 3.67 kOe and a maximum energy product $(BH)_{max}$ of 2.05 MG·Oe were obtained for $Mn_{54.5}Al_{30.5}Ga_{15}$ powders (Fig. 13). The observed magnetic properties are in accordance with the competing ferromagnetic interactions between Mn moments at the regular 1*a* site and antiferromagnetic coupling with the excess Mn atoms occupying the 1*d* site.

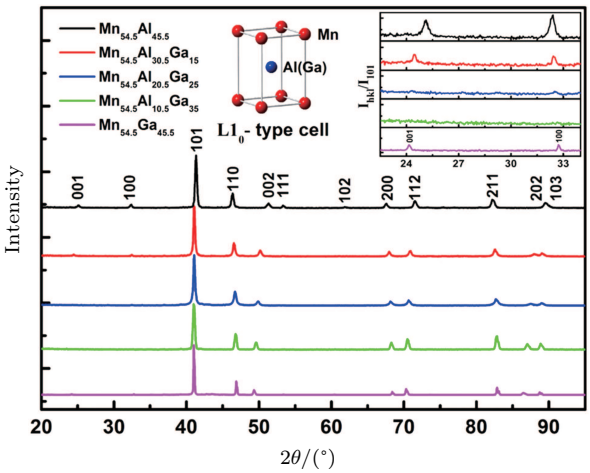


Fig. 11. (color online) XRD patterns of $Mn_{54.5}Al_{45.5-x}Ga_x$ ($x = 0.0$, 15.0, 25.0, 35.0, 45.5) samples. The right inset shows the magnified region around the (001) and (100) peaks, which are normalized by the intensity of the (101) peak.[18]

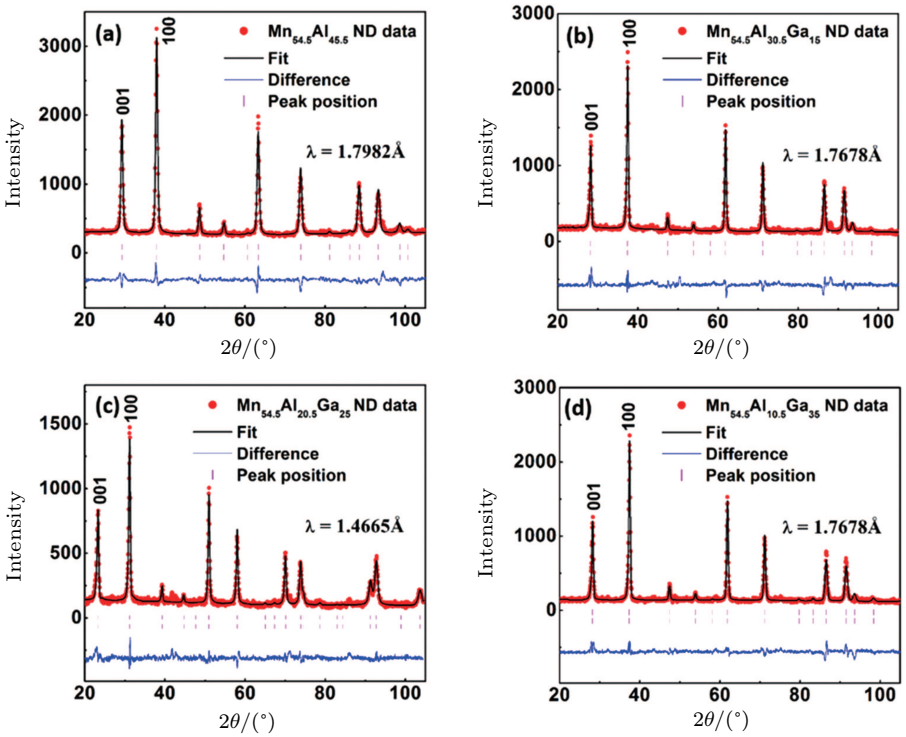


Fig. 12. (color online) Neutron diffraction patterns of the (a) $Mn_{54.5}Al_{45.5}$, (b) $Mn_{54.5}Al_{30.5}Ga_{15}$, (c) $Mn_{54.5}Al_{20.5}Ga_{25}$, and (d) $Mn_{54.5}Al_{10.5}Ga_{35}$ samples at 300 K, which are indexed to the $L1_0$ tetragonal structure. The simulated pattern (black line) is compared to experimental data (red dots). The difference is shown by the blue line. The structural and magnetic peak positions are shown by magenta bars.[18]

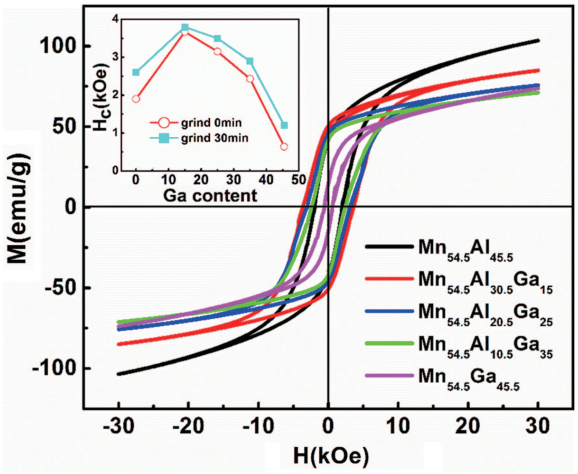


Fig. 13. (color online) Room temperature $M(H)$ hysteresis loops of $Mn_{54.5}Al_{45.5-x}Ga_x$ ($x = 0.0$, 15.0, 25.0, 35.0, 45.5) samples. The inset shows the coercivity as a function of Ga content with milling time of 0 and 30 min.[18]

3. MnBi hard magnetic materials

The MnBi low temperature phase (LTP) with an NiAs-type hexagonal crystal structure exhibits unique magnetic and structural properties. The saturation magnetization of LTP MnBi is about 81 emu/g at RT, and the maximum theoretical energy product $(BH)_{max}$ is about 18 MG·Oe. The magnetic anisotropy constant K is about 10^7 ergs/cm^{-3} at 500 K. Compared to those of most ferromagnetic materials, the unusual positive temperature coefficient of coercivity from 150 K to 550 K in the LTP MnBi makes it a promising candidate for applications as a high-temperature magnet.[33–40] Heusler first discovered the ferromagnetic MnBi over a century ago.[33] An energy product $(BH)_{max}$ of 4.3 MG·Oe was achieved in the 1950's.[34] The highest $(BH)_{max}$ of the bulk LTP MnBi magnet that has been observed to date is about 8–10 MG·Oe at room temperature,[40,41] which is mainly related to the fact that it is hard to obtain high purity MnBi powders, as Mn tends to segregate from the Mn–Bi liquid at the peritectic temperature. Considerable efforts have been expended to prepare high purity LTP MnBi over the past decades through methods including rapid solidification,[36,38] arc melting,[43] sintering,[44,45] mechanical alloying,[46] and chemical solution.[47] Over 95 wt.% was prepared by rapid quenching from melt followed by thermal annealing.[38] High purity MnBi powder ($> 90\%$) was obtained by sintering and exhibited an M_s of 74.6 emu/g at room temperature, while the $(BH)_{max}$ of the properly aligned powder reached 11.9 MG·Oe.[41] Ko *et al.*[45] fabricated MnBi magnets with a coercivity value of 10 kOe and $(BH)_{max}$ up to 5.34 MG·Oe using mechanically alloyed powders via the spark plasma-sintering process. At room temperature, the cryomilled powders show large coercivity values of 18.5 kOe and 20.7 kOe for $Mn_{50}Bi_{50}$ and $Mn_{55}Bi_{45}$, respectively.[48] Recently, by using low temperature low energy ball milling and fast warm compaction technique, a MnBi bulk magnet with a density of 8.4 g/cm^3 has been achieved, which exhibits a $(BH)_{max}$ of 7.8 MG·Oe at 300 K.[49] The hybrid anisotropic MnBi/$Sm_2Fe_{17}N_x$ magnet with a maximum energy product $(BH)_{max}$ of 18 MG·Oe at 300 K was also prepared.[50] As a hard phase in the hybrid magnets, MnBi could improve the temperature dependence of the hybrid magnets.[51,52]

To improve the hard magnetic property of MnBi, we have employed different methods to synthesize the high purity MnBi alloys.[37,38,42,50,53–57] (1) Sintering method: well mixtures of manganese (99.9%) and bismuth (99.99%) powders were molded into a columnar shape and then sintered in an argon atmosphere at 1000 °C for 24 h followed by cooling to room temperature. The optimum composition was about Mn:Bi = 55:45, at which 60 wt.% of LTP MnBi can be achieved after sintering. (2) Mechanical alloying: the mixed powders of appropriate amounts of Mn and Bi were mechanically alloyed, and subsequently annealed at 800 °C for 2 h. About 30 wt.% of LTP MnBi can be obtained by this method. (3) Induction/arc melting: the ingots of MnBi were prepared by induction/arc melting appropriate amounts of Mn and Bi under an argon atmosphere. About 20 wt.% of LTP MnBi can be obtained after induction melting. (4) Melt spinning: the ingots of MnBi were prepared by induction/arc melting appropriate amounts of Mn and Bi under an argon atmosphere. The ingots were then divided equally into several parts with each part about 2.5 g. The ribbons of Mn_xBi_{100-x} were obtained by ejecting the melt from a quartz tube onto the surface of a rotating copper wheel under an argon atmosphere. The tangential speed of the wheel was altered from 10 m/s to 70 m/s. The ribbons were then annealed at different temperatures from 473 K to 773 K. To improve the purity of LTP MnBi, the as-prepared alloys were crushed into powders, and a magnetic separation process was then employed to enrich the LTP MnBi. According to the XRD and ND data refinements,[42] the ratio of LTP MnBi can be enriched up to about 90 wt.%, 60 wt.%, and 25 wt.% after magnetic separation for methods (1), (2), and (3), respectively. It is obvious that method (1) is more suitable for producing high-purity LTP MnBi, which is probably owing to the good reactivity between Mn and Bi, and the larger grain size, which facilitates the magnetic separation.

To improve the hard magnetic properties of MnBi, the magnetic separated powders from method (1) are further pulverized into fine particles approaching a single domain size of about 500 nm. The fine powders are fixed into an epoxy resin under a magnetic field of about 1.0 T to form aligned samples of cylindrical shape. The hysteresis loops of resin-bonded MnBi powders measured at different temperatures are shown in Fig. 14(a). Coercivities of 2.0 T and 1.5 T were observed at room temperature and 400 K, respectively. Below 150 K, the coercivity tends to become zero owing to the spin reorientation of the Mn atomic moments (see Fig. 14(b)). The maxi-

mum energy products $(BH)_{max}$ of the magnet are 7.7 MG·Oe (61 kJ/m^3) and 4.6 MG·Oe (37 kJ/m^3) at room temperature and 400 K, respectively. As shown in Fig. 14(b), the coercivity rapidly increases with temperature from 150 K to 400 K, and an even larger coercivity than 2.0 T can be expected at a higher temperature. This is a great advantage for high-temperature applications relative to most of the present hard magnets such as $Nd_2Fe_{14}B$, which has a negative coefficient.

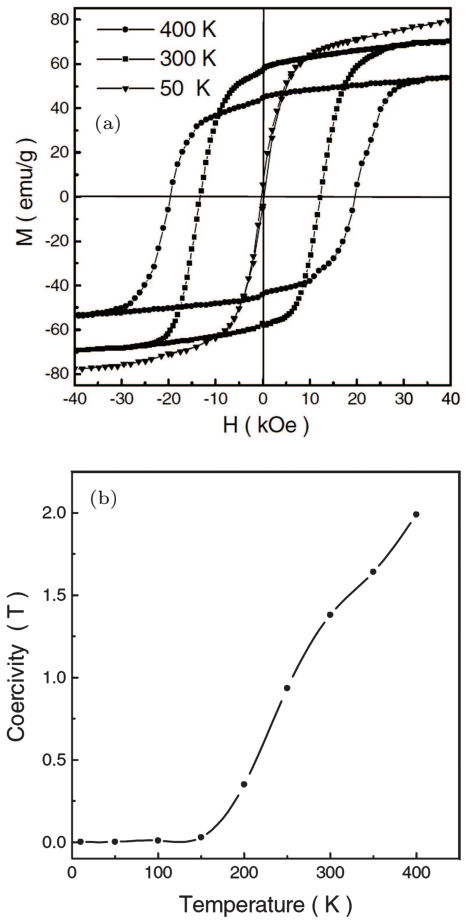


Fig. 14. (a) The hysteresis loops of resin-bonded MnBi magnets measured at different temperatures, and (b) the coercivity at different temperatures.[42]

Melt spinning is a method that can produce nanosize MnBi grains with high purity, as it can reduce or even eliminate Mn segregation, i.e., avoid the segregation by preparation of an amorphous MnBi precursor.[38] MnBi ribbons with different compositions were prepared at various quenching rates.[54,55] It was found that the ribbons that quenched at 60 m/s showed a complete amorphous phase. The low speed (10 m/s) quenched ribbons have an inhomogeneous fraction, which shows distinct peaks of Mn and Bi in the XRD patterns. Thus, a high wheel speed of 65 m/s was used to obtain the amorphous ribbons. The ribbons were annealed in the temperature range of 473 K to 893 K. Figure 15 is the XRD pattern of $Mn_{55}Bi_{45}$ melt-spun at 65 m/s before and after annealing. It can be seen from the pattern that amorphous MnBi transforms to high purity LTP MnBi at 573 K. The content of MnBi determined from XRD and ND data is higher than 95%. A saturation magnetization of 75 emu/g was measured at room temperature. It was also found that when $Mn_{55}Bi_{45}$ was used in the mixture, LTP MnBi with a purity of more than 95 wt.% could be stably prepared after annealing.

The SEM image (Fig. 16(a)) indicates that the grain size is on a nanoscale for the as-prepared ribbons. For the annealed ribbons, an average grain size of about 20–30 nm was observed by TEM, as shown in Fig. 16(b). To improve the magnetic properties, the annealed ribbons were milled for various durations. The SEM images of the milled MnBi magnetic powders are shown in Figs. 16(c) and 16(d). The size of the MnBi particle is about several microns as seen in

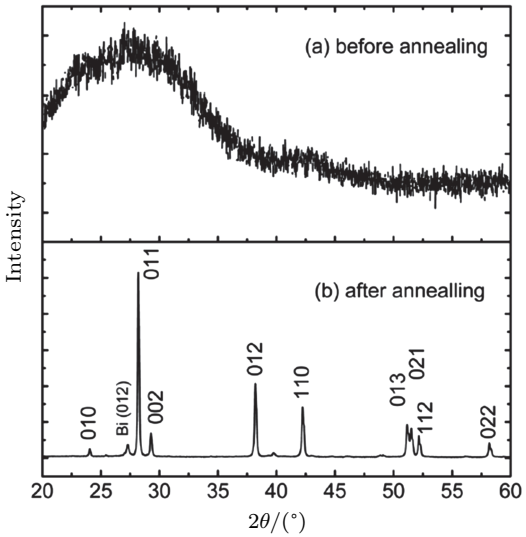


Fig. 15. XRD patterns of the MnBi after melt spinning at a speed of 65 m/s (a) and subsequently annealing at 573 K for 3 h (b).[38]

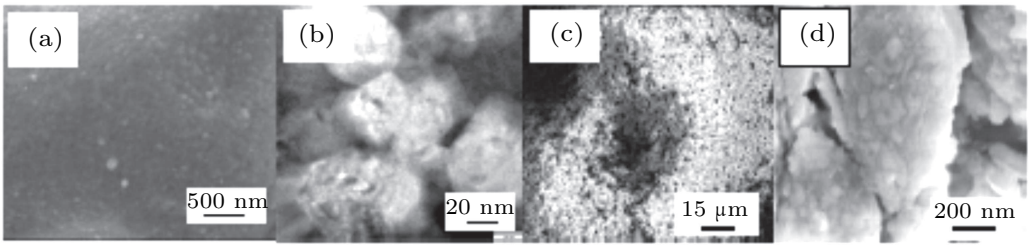


Fig. 16. (a) SEM image of as-quenched MnBi ribbons melt-spun at 65 m/s, (b) TEM image of annealed ribbons melt-spun at 65 m/s, (c) and (d) the milled MnBi powders.[38]

Fig. 16(c). The particle morphology observed after magnification (Fig. 16(d)) indicates that each of the large MnBi particles contains a number of small grains. This indicates that the size of the MnBi grains is much smaller than the size of the particles after milling. As the MnBi single domain size is around 500 nm, the resulting grains can be regarded as single domain size grains.

Figure 17 plots the hysteresis loops of the milled powders measured at different temperatures. The ratio of the remanence to saturation magnetization M_r/M_s is about 0.935, which indicates that most of the particles are aligned to the c-axis. As most nanocrystalline magnets prepared by melt spinning are isotropic and show an M_r/M_s ratio of normally less than 60%, such a high M_r/M_s ratio of nanocrystalline MnBi is unique and is due to to the crystallographically orientation of the single crystal grains. The coercive forces reach 1.9 T and 1.1 T at 400 K and 300 K, respectively. The maximum energy products $(BH)_{max}$ are 8.9 MG·Oe (70 kJ/m^3) and 5.0 MG·Oe (40 kJ/m^3) at room temperature and 400 K, respectively. The coercivity and energy product are much larger than those of the $Nd_2Fe_{14}B$ magnet at 400 K, and have a very low temperature coefficient. Figure 18 is the temperature dependence of the coercivity for the powders milled for 7 h. The coercivity of MnBi increases with temperature from 100 K to 540 K, reaches a maximum of 2.5 T at 540 K, and then decreases slowly to 1.8 T at 610 K. The positive temperature coefficient of the coercivity is related to the magnetocrystalline anisotropy field of MnBi, which increases with temperature from 150 K to 530 K, and reaches a maximum at about 530 K.[35,36]

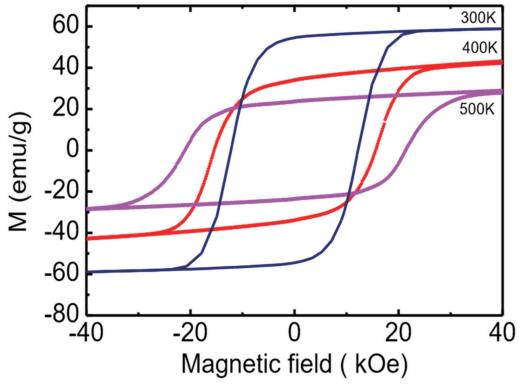


Fig. 17. (color online) Hysteresis loops of the milled powders measured at different temperatures.[38]

The powder neutron diffraction was used to investigate the phase and structural evolution of MnBi with different temperatures.[37,38] The temperature dependence of lattice parameters, c/a ratio, and magnetic moment of MnBi obtained from refined ND data are summarized in Fig. 19. A kink is observed in both the a and c axes around 100 K, which is consistent with the spin reorientation of the Mn atoms observed in Fig. 20. The relaxation of the lattice is found to be associated with changes in the magnetocrystalline anisotropy from planar to c-axis anisotropy. When the c/a ratio is less than 1.425, the LTP MnBi shows planar anisotropy; as $c/a > 1.425$, the uniaxial anisotropy appears, and the anisotropic field increases with an increase in c/a up to 1.433. When the c/a ratio reaches 1.433, a magnetostructural phase transition from ferromagnetic to paramagnetic occurs. At the magnetostructural transition, the c/a ratio of the nanostructured MnBi remains unchanged, whereas that of the bulk material decreases abruptly to 1.37. No evidence of discontinuity is noticed for the lattice a- and c-parameters at 625 K for high purity MnBi, while the discontinuity is easily seen in the lattice parameters of the bulk at this temperature. The magnetic moment of the Mn atom decreases slowly with an increase in temperature (Fig. 19(b)) and shows no discontinuity around 100 K corresponding to the spin reorientation of the Mn atom. A sharp drop in the magnetic moment is observed at 540–550 K owing to the magnetic phase transition, and it reaches a value of 1.41 μ_B at 600 K.

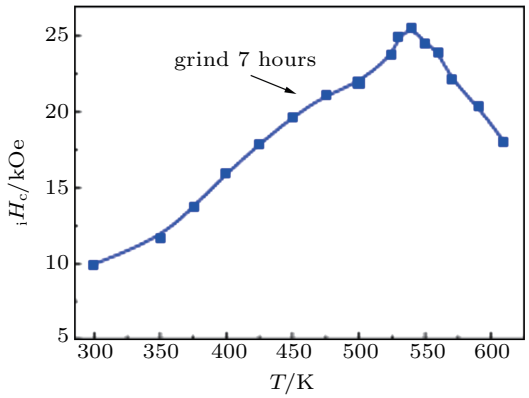


Fig. 18. (color online) Temperature dependence of the coercivity for LTP MnBi.[38]

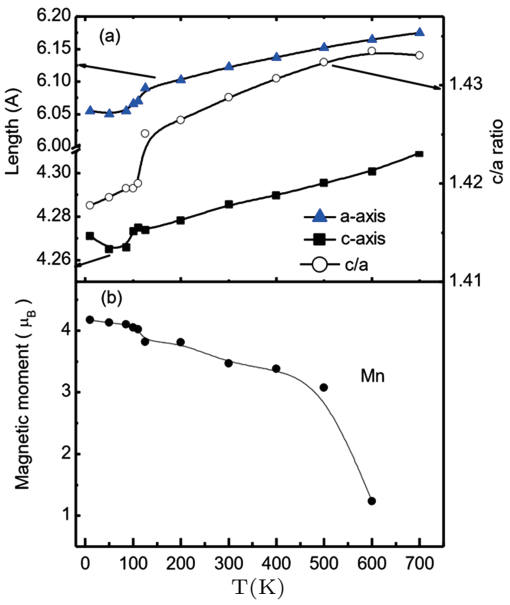


Fig. 19. (color online) (a) Lattice parameters a, c, and c/a ratio of MnBi at different temperatures, and (b) the temperature dependence of the Mn magnetic moment in MnBi.[38]

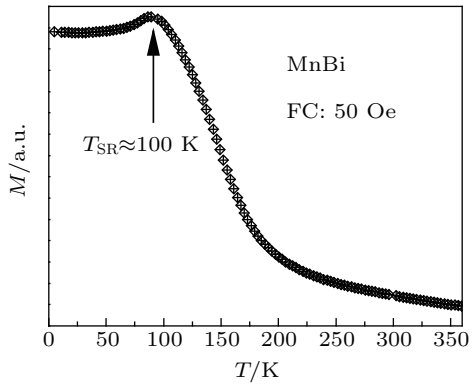


Fig. 20. Thermo-magnetic curve of MnBi measured along the *c*-axis.

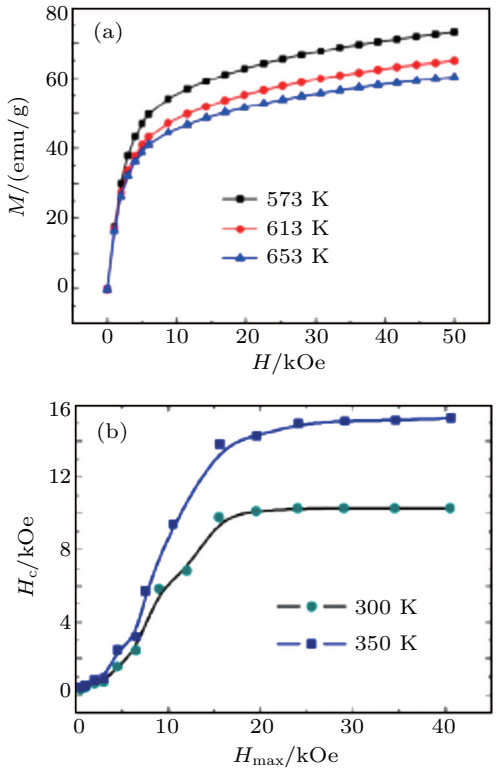


Fig. 21. (color online) (a) Initial magnetization curves for MnBi with different annealing temperatures. (b) Relationship between coercivity field and maximum applied magnetic field at 300 K and 350 K.

The coercivity mechanism of MnBi can be simply analyzed by using the initial magnetization curves of MnBi magnetic powders. As shown in Fig. 21, when the applied magnetic field is small, the magnetization increases rapidly to near saturation, and this phenotype is the nucleation controlled magnetizing mode. In the magnetization process, rotation of the magnetic moment and movement of the magnetic domain are the main occurrences. Obvious domain wall pinning behavior is not observed. The initial magnetization curves of 573 K, 613 K, and 653 K of the annealed samples are very steep. To study the coercivity mechanism under the nucleation model, the relationship between the coercivity and the applied field was measured (see Fig. 21(b)). From the curves of the coercivities measured at 300 K and 350 K, one can see that the coercivities increase with the applied magnetic field and slowly reach their maximum values. The curve is not perfectly linear owing to microstructural factors such as grain misalignment and lattice defects in the materials.

A more in-depth analysis of the coercivity mechanism was conducted using the micromagnetic theory.[55,56] The angular dependence of coercivity is determined from the hysteresis loops measured at different angles and shown in Fig. 22(a). The coercivity decreases with an increase in the angle between the easy axis and the applied field direction, indicating that a coherent rotation of magnetization occurs in MnBi according to the classical Stoner–Wohlfarth (S–W) model.[58] The mechanism of coercivity was then analyzed by comparing the experimental results with three theoretical models: (i) the S–W model with H_N^{ideal} ($K_1 \neq 0$, $K_2 = 0$, $K_3 = 0$) for $K_2 = 0$ and $K_d = 0$ originally proposed by Stoner and Wohlfarth, where the parameters K_1 and K_2 are the anisotropy constants of MnBi, and K_d is the anisotropy constant related to the demagnetization field; (ii) the nucleation field model developed by Kronmüller *et al.*[59] that considers the second anisotropy constant K_2 ($K_2/K_1 = 0.318$ for MnBi at room temperature,[60] as shown in the H_N^{ideal} ($K_1 \neq 0$, $K_2 \neq 0$, $K_d = 0$) curve; (iii) for the third model,[61] ${}_iH_c^{Pin}$ represents the angular dependence of the pinning field, which is proportional to $1/\cos\theta$. The angular dependence of the theoretical nucleation and pinning fields for ideal grain alignment are plotted in Fig. 22(b). The value of the *y* axis is normalized to the value for $\varphi = 0$. The angular dependence of the critical field H_N and coercive field ${}_iH_c$ of MnBi measured at 300 K are also plotted in Fig. 22(b). Here, the critical field H_N is defined as the point of inflection of the hysteresis loops in the second or third quadrant, and the coercive field ${}_iH_c$ is defined as the magnetic field where the magnetization is zero. It is found that H_N^{exp} initially decreases with increasing φ, and then increases from $\varphi = 45°$ to 90°, which is at most coincident with the H_N^{ideal} ($K_1 \neq 0$, $K_2 = 0$, $K_d = 0$) curve. The disparity in H_N between the experimental measurement and Stoner–Wohlfarth model may be caused by not including the second anisotropy constant K_2, which will increase the critical field.[56] In addition, the coercive field ${}_iH_c^{exp}$ shows a different dependence on φ. The variation trend of ${}_iH_c^{exp}$ is in accordance with that of H_N^{exp} for $0° \leq \varphi \leq 45°$. However, H_c^{exp} starts to deviate from H_N^{exp} in the range of $45° \leq \varphi \leq 90°$, which was predicted by the Stoner–Wohlfarth model. Therefore, the magnetic reverse process of MnBi powders is supposed mainly controlled by coherent rotation of single domain grains. Because the grain sizes in LTP MnBi do not show an apparent change from 300 K to 540 K, the Stoner–Wohlfarth model is supposed to be the appropriate coercivity mechanism for MnBi at temperatures between 300 K and 540 K.

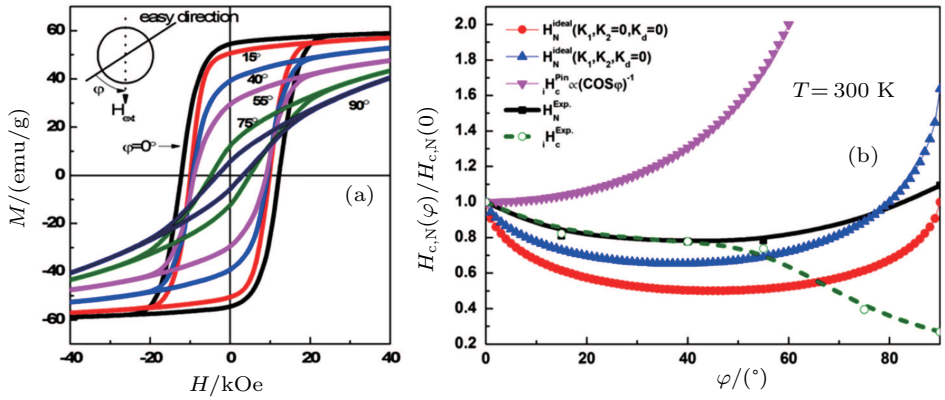


Fig. 22. (color online) (a) Hysteresis loops of MnBi anisotropic powders measured at various angles, taken at 300 K. (b) The theoretical angular dependence of the Stoner different model, the nucleation field model developed by Kromuller, and the $1/\cos\varphi$ law. The experimental results for the coercive field ${}_{\mathrm{i}}H_{\mathrm{c}}$ and critical field H_{N} of 7 h milled MnBi powder measured at 300 K.[55]

4. Mn_xGa magnetic materials

Mn–Ga exhibits remarkable magnetic properties with different structures. Mn–Ga forms mainly two kinds of crystal structures, the tetragonal $L1_0$ (tP4; $P4/mmm$; AuCu) and $D0_{22}$ (tI8; $I4/mmm$; Al_2Ti) types, depending on the composition.[62–65] $Mn_{3x}Ga$ compounds with $D0_{22}$ ($0.0 \leq x \leq 1.1$) and $L1_0$ ($1.2 \leq x < 2.0$) structures are expected to have anisotropy constants K_{u} of 20 Mergs/cm^3 and 26 Mergs/cm^3, magnetizations M_{s} of 305 emu/cm^3 and 845 emu/cm^3, and energy products $(BH)_{\max}$ of 3.67 MG·Oe and 28.2 MG·Oe, respectively.[65–67] For $L1_0$-type MnGa alloys, the key issue is that the ${}_{\mathrm{i}}H_{\mathrm{c}}$ value is still relatively low. The coercivity of the $Mn_{1.2}Ga$ ribbon was only about 1.0 kOe, although the anisotropy constant of 14.0 Merg/cm^3 was measured.[68] Another problem is that the Mn–Ga powder can only be aligned partially and the hot compacted sample is isotropic.[69] Owing to the low magnetization and the high material cost of Ga, $D0_{22}$-type Mn–Ga is not suitable for permanent magnetic applications. However, it can be a valid candidate for spintronics and the hard component of an exchange spring magnet.

To understand the magnetic properties, Krén *et al.* first revealed the ferrimagnetic structure of $D0_{22}$-type Mn–Ga using neutron diffraction experiments, with Mn magnetic moments of 1.6 μ_{B} at the 4*d* site and 2.8 μ_{B} at the 2*b* site.[70] To explain the compositional dependence of magnetic properties for $D0_{22}$-type Mn–Ga alloys, Mizukami *et al.* have proposed a magnetic structure model in which the extra Mn atoms can randomly replace Ga atoms at the 2*a* or 2*b* sites and couple antiferromagnetically with the Mn atoms at the 4*d* site in Mn–Ga films.[71] Winterlik *et al.* proposed the Mn atom vacancy model involving the Mn vacancies at both the 2*b* and 4*d* sites.[72] Normally, the vacancies at the 2*b* or 4*d* sites will decrease *c* and the unit cell volume *V*, but the observed experimental data show that *c* and *V* increase with a decrease in Mn content. Recently, Rode *et al.* obtained a noncollinear magnetic structure in Mn_3Ga, where the 2*b* moment has a soft intrinsic *a*–*b* plane component.[73] The structural correlation and transformation between are not well studied, which is critical for understanding the magnetic properties of these compounds. Therefore, a symmetrical investigation of the crystal and magnetic structures of the Mn_xGa compounds for the wide composition range is required.

We have used several different methods to synthesize the ferro/ferrimagnetic Mn–Ga alloys:[74,75] (i) Mn_xGa ($1.0 \leq x \leq 3.0$) alloy ingots were prepared by arc melting method. We found that it is generally difficult to obtain a single-phase magnetic phase by annealing the bulk ingot directly. To promote the magnetic phase, we first mechanical crushed the ingots into powders, and then heat-treated the alloy powders. For Mn_xGa ($x = 1.2$, 1.4, 1.6) powders, heat treatment at 350–500 °C can directly lead to a magnetic phase, and the higher the temperature, the shorter the heat treatment time required. While for Mn_xGa ($x = 1.8$–3.0) alloys, ingots were first sawed into powder (different from the previous mechanical crushing), and the resulting γ-Mn phase sawdust was then transformed into tetragonal $D0_{22}$ phases by annealing at 400 °C for 14 d. (ii) Mn_xGa ($x = 1.8$–3.0) ingots were melt-spun at a rate of 15 m / s, and the resulting ribbons were then heat treated. It was found that the main phase in the Mn_xGa ($x = 1.8$–2.6) ribbons is the η phase of $D0_{19}$, while $Mn_{2.8}Ga$ and $Mn_{3.0}Ga$ ribbons are all in γ phase. All ribbon samples were annealed at 400 °C for 7 d to form a single tetragonal phase.

Figure 23 shows the XRD patterns of the prepared Mn_xGa ($x = 1.2$–3.0) magnetic phases. Some of them are do not appear in all of the Mn–Ga phase diagrams.[76–80] The range of the Mn atomic fraction of the Mn–Ga magnetic phase we have obtained is the largest reported in the literatures. All diffraction peaks can be indexed to a single tetragonal phase: the $D0_{22}$ or $L1_0$ phase (see Fig. 24). The magnetic phase of Mn_xGa ($x < 2.0$) has an $L1_0$ structure and that of Mn_xGa (> 2.0) has a $D0_{22}$ structure. These two structures look very similar. If a cell of $D0_{22}$ is regarded as a supercell of the $L1_0$ unit cell, which extends twice along the *c*-axis, the difference in the two is essentially only the ordering degree of the atom

occupying position. From the XRD patterns of the $D0_{22}$- and $L1_0$-type structures, it is obvious that the two kinds of diffraction spectra are almost identical, except in the low angle region (20°–35°) in Fig. 23(b), where the (101) peak from $D0_{22}$ structure can be used to distinguish them. The three peaks with the indexes of (002), (101), and (110) are crucial as they can be used to identify the structural evolution and occupation fraction of the specific atomic sites in the tetragonal structure. Owing to the poor x-ray contrast between Mn and Ga, and the weak intensities of the typical peaks, the XRD pattern cannot be used to study the Mn–Ga atomic site disordering effect in these compounds. Hence, the exact atomic occupation can only be further refined using neutron diffraction data.

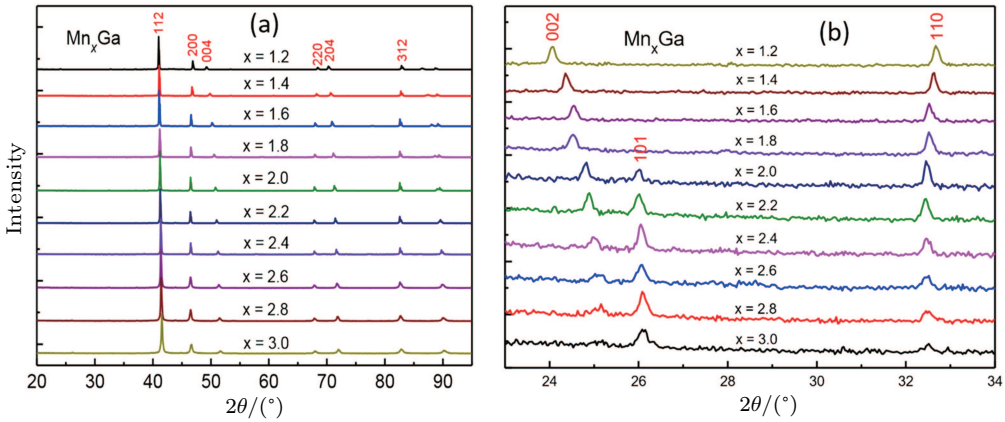


Fig. 23. (color online) (a) Typical room temperature XRD patterns of Mn_xGa ($1.2 \leq x \leq 3.0$); (b) enlarged low angle region of the XRD patterns.

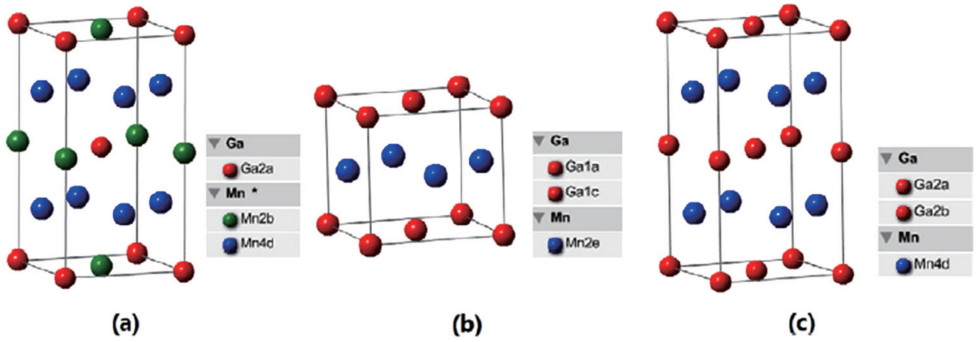


Fig. 24. (color online) (a) The tetragonal $D0_{22}$ structure. (b) The tetragonal $L1_0$ structure. (c) The tetragonal $D0_{22}$ structure, including two unit cells with $L1_0$ structure.[75]

To further analyze the crystal and magnetic structures of Mn_xGa, the ND patterns of Mn_xGa ($x = 1.2$–3.0) were collected and are shown in Fig. 25. Different from the XRD patterns in Fig. 22, the typical peaks (101) and (110) become the strongest peaks owing to the pronounced scattering length difference between Mn and Ga atoms (i.e., $b_{Mn} = -0.373$, $b_{Ga} = 0.729$, both in units of 10^{12} cm) in the ND pattern. Three peaks, i.e., (002), (101), and (110), provide the ordering degree of the atom occupying position and the contribution from the magnetic structure.

According to the XRD and neutron diffraction data analyses,[18,74] we hypothesized that Mn_3Ga had an ideal $D0_{22}$ structure and that a decrease in Mn content would lead to the substitution of the excess Ga by Mn. Mn_xGa ($2.2 \leq x \leq 2.8$) also has a $D0_{22}$-like structure. Mn_2Ga and $Mn_{1.8}Ga$ belong to the transition region from a $D0_{22}$ structure to an $L1_0$ structure, in which not only 2*b*-Mn is substituted by Ga, but 2*a*-Ga is substituted by Mn. Mn_xGa ($1.2 \leq x \leq 1.6$) compounds have an $L1_0$ structure. All of the above structures can be described by a $D0_{22}$ supercell model in which 2*a*-Ga and 2*b*-Mn are simultaneously substituted.[74] We used this structural model to sufficiently fit all the neutron diffraction spectra of Mn_xGa ($1.2 \leq x \leq 3.0$) in Fig. 25. The refined occupancy numbers of Mn and Ga atoms at different sites are shown in Fig. 26. As the Mn content decreases, the occupancy number of the 2*b*-site Mn atom decreases from 2.0 to 0.2. At the same time, the occupancy number of the 2*b*-site Ga atom increases from 0.0 to 1.8. As expected from the analysis, as the Mn content decreases, the structure gradually transforms from a $D0_{22}$ structure to an $L1_0$ structure. In this process, the 2*b*-site Mn atoms are gradually replaced by 2*a*-site Ga atoms, increasing the disorder of these two sites. When x decreases to 1.8, the atomic ratio of the Mn atoms at the 2*a* and 2*b* sites (i.e. r_{Mn}) is the same as that of the Ga atoms (i.e., r_{Ga}). Further, as x

decreases, the same ratio (i.e., $r_{Mn} = r_{Ga}$, namely, the structural form factor $f_{2a} = f_{2b}$) is maintained. It is notable that the refined occupancy numbers for $Mn_{1.8}Ga$ and $Mn_{2.0}Ga$ are located between the two model values, indicating that the atomic ratio of Mn (Ga) atoms at 2*a* and 2*b* sites is almost the same in this transition region.

Figure 26(c) shows the lattice parameters obtained from the ND data. With the increase in *x*, parameter *a* remains almost constant, and *c* shows a significant increase, resulting in an increase in unit cell volume *V*. Our experimental data imply that *V* and density ρ increase linearly with a decrease in Mn content, which indicates that Mn atoms are replaced by Ga atoms and do not form atomic vacancies with increasing *x*. This is different from Winterlik's model that involves the Mn vacancies at the 2*b* sites or at both the 2*b* and 4*d* sites for $Mn_{3-x}Ga$ alloys.[72] This agrees with the report by Mizukami *et al.*, in which the authors mentioned that Mn vacancies were not observed in their Mn_xGa_{1-x} films.[71] The refined magnetic moments from the ND data (see Fig. 27(a)) are consistent with the magnetic measurements, which further support this. As *x* increases, the moment at the 4*d* site remains at about 2.2 μ_B, while the moment of the Mn atom at the 2*b* site increases from 2.3 μ_B to 3.3 μ_B (Fig. 27(b)) and shows antiferromagnetic coupling to that at 4*d* sites shown in the inset of Fig. 27(a).

Figure 28(a) is the normalized magnetization ($M/M_{300\ K}$) as a function of temperature for the Mn_xGa samples. When $1.2 \leq x \leq 2.4$, the Curie temperature increases linearly from 550 K to 761 K with an increase in Mn content (Fig. 28(b)). However, there is an anomaly for Mn_xGa with $x = 2.6$, 2.8, and 3.0, and the Curie temperature does not increase continuously. The high temperature XRD measurements of these three samples indicate that Mn_xGa ($2.6 \leq x \leq 3.0$) transforms

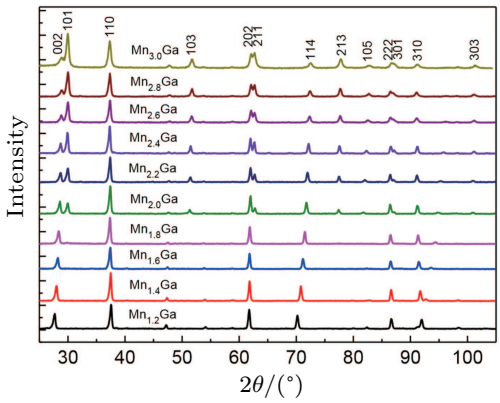


Fig. 25. (color online) Neutron diffraction patterns of Mn_xGa at RT.[74]

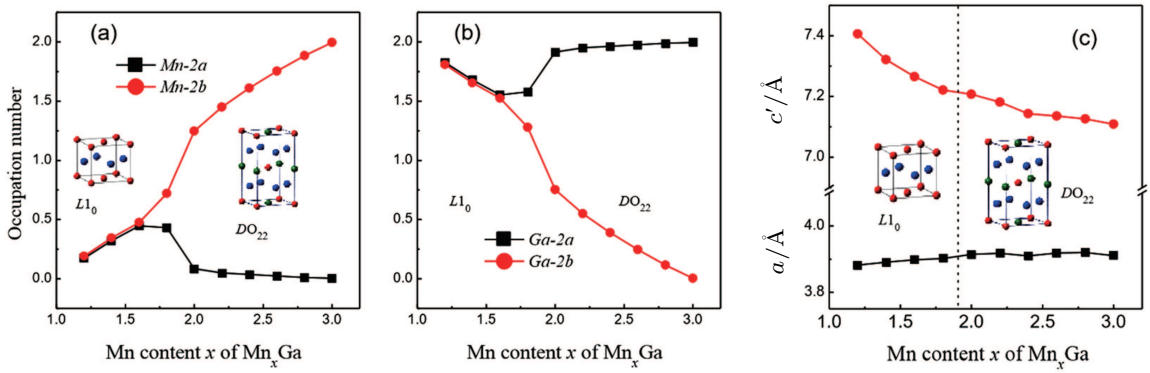


Fig. 26. (color online) Obtained occupation numbers of (a) Mn and (b) Ga atoms at different sites, and (c) the refined lattice parameters *a* and c' of Mn_xGa (c' is twice *c* of the $L1_0$ cell).[74]

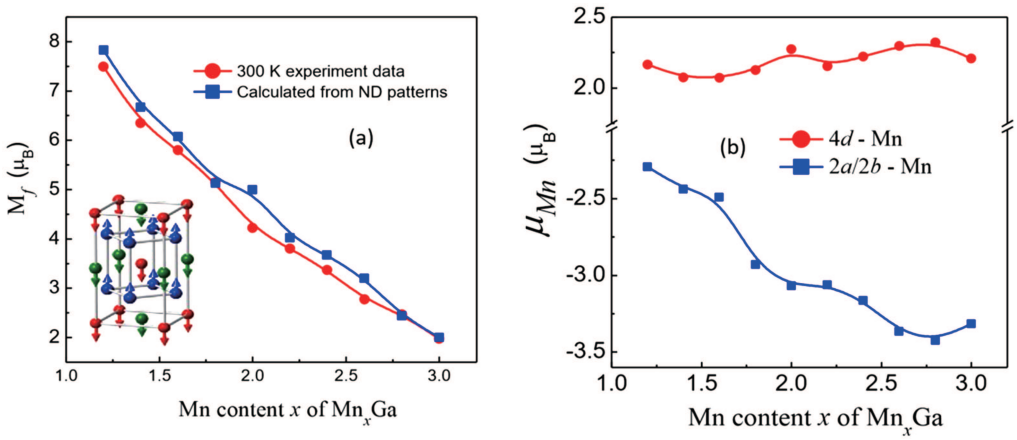


Fig. 27. (color online) (a) Refined magnetic moments of the unit cell from the refined ND data and (b) refined magnetic moments of Mn atom (μ_{Mn}) at $2b/2a$ site and 4*d* site versus *x*.[74]

from a magnetic phase with a $D0_{22}$ structure to a nonmagnetic phase with a $D0_{19}$ structure around 760 K. In addition, the magnetization increases with an increase in temperature when $2.6 \leq x \leq 3.0$, which is related to the ferrimagnetic exchange interaction in the Mn_xGa ($2.6 \leq x \leq 3.0$) due to the antiferromagnetic coupling between Mn atoms at 1*a* and 4*d* sites.

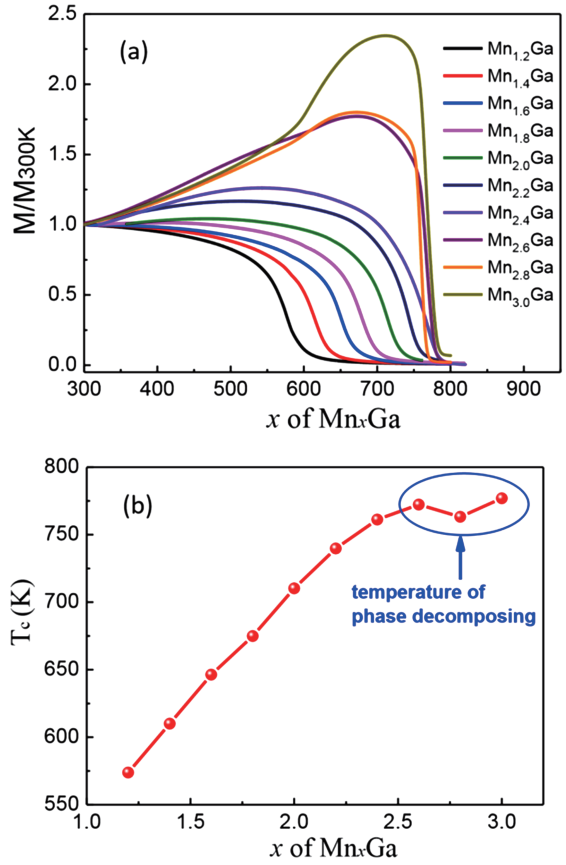


Fig. 28. (color online) (a) Normalized magnetization versus temperature curves of Mn_xGa ($1.2 \leq x \leq 3.0$) (applied field 1 T) and (b) the Curie temperatures of the Mn_xGa.[74]

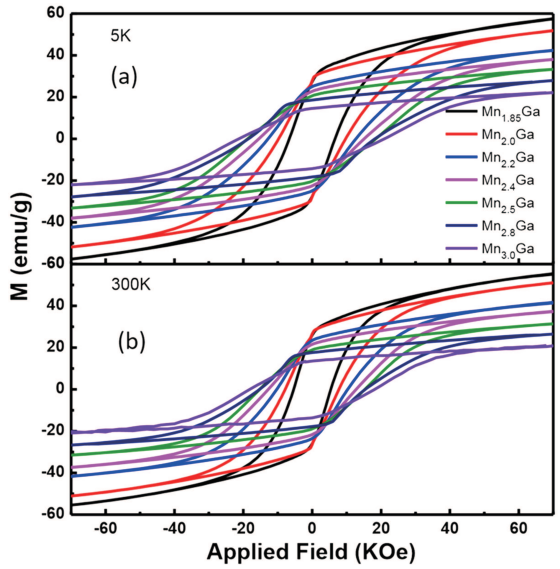


Fig. 29. (color online) Hysteresis loops of Mn_xGa at the temperatures of (a) 5 K and (b) 300 K.[75]

The Mn_xGa ($x = 1.8$–3.0) powders prepared by the annealing of ingot powders have very high coercivity.[74] The hysteresis loops of the annealed $Mn_{3-x}Ga$ samples measured at 5 K and 300 K are displayed in Fig. 29. All the samples show wide $M(H)$ hysteresis loops, but the magnetizations are not saturated even at 70 kOe. This suggests that $Mn_{3-x}Ga$ powders have relatively large magnetic anisotropy. The magnetization and coercivity are very sensitive to the composition of $Mn_{3-x}Ga$ (Figs. 29 and 30). The maxima of the magnetic moments (at 7 T) of the series clearly increase from 22.3 emu/g to 57.4 emu/g at 5 K, and 21 emu/g to 55.5 emu/g at 300 K as x increases from 0 to 1.15. The coercivity ${}_{\rm i}H_{\rm c}$ of Mn_xGa increases from 6.6 kOe to 21.4 kOe at 5 K and from 5.4 kOe to 18.2 kOe at 300 K with increasing x (see Fig. 30). This coercivity is much higher than that of any other bulk Mn_xGa ever reported. This is related to the microstructure of the powders.[75]

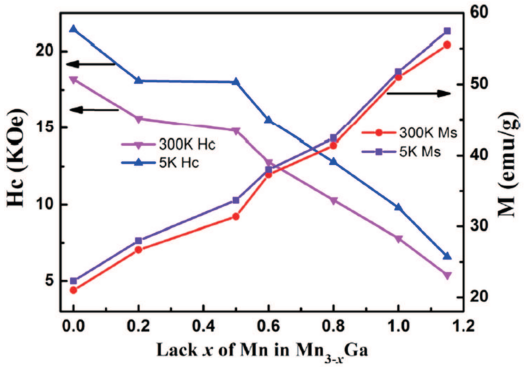


Fig. 30. (color online) Composition dependence of the saturation magnetization $M_{\rm s}$ in a 7 T field and the coercivity ${}_{\rm i}H_{\rm c}$ of Mn_xGa at the temperatures of 5 K and 300 K.[75]

5. Summary

In this work, the magnetic and structural properties of Mn-based intermetallic compounds (MnX, where X = Al, Bi, and Ga) have been reviewed. We successfully produced magnetic single phases of MnAl, MnBi, and Mn_xGa using different methods. A saturation of 125 emu/g, coercivity of 5 kOe, and maximum energy product $(BH)_{\rm max}$ of 3.1 MG·Oe were achieved at room temperature for the pure τ-Mn–Al magnetic powders without carbon doping and an extrusion process. The maximum energy products $(BH)_{\rm max}$ of LTP MnBi were 8.9 MG·Oe (70 kJ/m^3) and 5.0 MG·Oe (40 kJ/m^3) at room temperature and 400 K, respectively. The coercivity of MnBi increased with temperature from 100 K to 540 K, and reached a maximum of 2.5 T at 540 K. The tetragonal $D0_{22}$ phases of the Mn_xGa showed relative high coercivities ranging from 7.2 kOe for low Mn content, i.e., $x = 1.8$, to 18.2 kOe for high Mn content, i.e., $x = 3$, at room temperature. A room temperature magnetization value of 80 emu/g can be achieved for the $Mn_{1.2}Ga$ sample. The hard magnetic properties of ${}_{\rm i}H_{\rm c} = 3.5$ kOe, remanence $M_{\rm r} = 43.6$ emu/g,

and $(BH)_{\max} = 2.5$ MG·Oe were obtained at room temperature. Based on the above investigations, we can conclude that Mn-based magnets can exhibit high Curie temperature, high magnetocrystalline anisotropy, and very high coercivity. The coercivities of MnAl alloys need to be further improved for practical applications by understanding their coercivity mechanism. Mn-based magnets such as LTP MnBi have great application potential as high temperature permanent magnets with a $(BH)_{\max}$ better than that of an $Nd_2Fe_{14}B$ magnet above 400 K. It is noticed that the relatively low magnetization of the Mn-based magnetic phase restricts them for real application as permanent magnets at room temperature. This can be tuned by forming new uniaxial structures with more elements. In addition, the prospects of exchange-spring magnets using Mn-based alloys as hard magnetic phases can also be used to further enhance their magnetic performance as novel magnetic materials.

Acknowledgement

The authors thank the Key Laboratory of Neutron Physics of CAEP for providing the neutron beam time.

References

[1] Strnat K 1970 *IEEE Trans. Magn. Mag.* **6** 182
[2] Croat J J, Herbst J F, Lee R W and Pinkerton F E 1984 *Appl. Phys. Lett.* **44** 148
[3] Sagawa M, Fujimura S, Togawa N, Yamamoto H and Matsuura Y 1998 *J. Appl. Phys.* **55** 2083
[4] Yang Y C and Zhang X D 1990 *J. Rare Earth* **4** 376 (in Chinese)
[5] Coey J and Sun H 1990 *J. Magn. Magn. Mater.* **87** L251
[6] Gutfleisch O, Willard M A, Brück E, Chen C H, Sankar S G and Liu J P 2011 *Adv. Mater.* **23** 821
[7] Coey J M 2012 *Scri. Mater.* **67** 524
[8] Coey J M 2014 *J. Phys.: Condens. Matter* **26** 064211
[9] Kōno H 1958 *J. Phys. Soc. Jpn.* **13** 1444
[10] Koch A J J, Hokkeling P, V dS M G and DeVos K J 1960 *J. Appl. Phys.* **31** S75
[11] Moze O, Pareti L and Ermakov A E 1988 *J. Appl. Phys.* **63** 4616
[12] Braun P B and Goedkoop J A 1963 *Acta Crystallogr.* **16** 737
[13] Konstantinović J, Popov D, Nešković N B and Popovici M 1978 *Solid State Commun.* **25** 337
[14] Yang Y, Ho W, Lin C, Yang J, Zhou H, Zhu J, Zeng X, Zhang B and Jin L 1984 *J. Appl. Phys.* **55** 2053
[15] Pareti L, Bolzoni F, Leccabue F and Ermakov A E 1986 *J. Appl. Phys.* **59** 3824
[16] Park J H, Hong Y K, Bae S, Lee J J, Jalli J, Abo G S, Neveu N, Kim S G, Choi C J and Lee J G 2010 *J. Appl. Phys.* **107** 09A731
[17] Hoydick D P, Palmiere E J and Soffa W A 1997 *J. Appl. Phys.* **81** 5624
[18] Zhao H, Yang W Y, Shao Z Y, Tian G, Zhou D, Chen X P, Xia Y H, Xie L, Liu S Q, Du H L,Han J Z, Wang C S, Yang Y C and Yang J B 2016 *J. Alloys Compd.* **680** 14
[19] Shao Z, Zhao H, Zeng J, Zhang Y, Yang W, Lai Y, Guo S, Du H, Wang C, Yang Y and Yang J 2017 *AIP. Adv.* **7** 056213
[20] Liu Z W, Chen C, Zheng Z G, Tan B H and Ramanujan R V 2012 *J. Mater. Sci.* **47** 2333
[21] Singh N, Mudgil V, An, K, Srivastava A K, Kotnala R K and Dhar A 2015 *J. Alloys Compd.* **633** 401
[22] Jimenez-Villacorta F, Marion J L, Oldham J T, Daniil M, Willard M A, Lewis L H 2014 *Metals* **4** 8
[23] Chaturvedi A, Yaqub R and Baker I 2014 *J. Phys.: Condens. Matter* **26** 064201
[24] Wei J Z, Song Z G, Yang Y B, Liu S Q, Du H L, Han J Z, Zhou D, Wang C S, Yang Y C, Franz A, Többens D and Yang J B 2014 *AIP. Adv.* **4** 182
[25] Lu W, Niu J, Wang T, Xia K, Xiang Z, Song Y, Zhang H, Yoshimura S and Saito H 2016 *J. Alloys Compd.* **675** 163
[26] Fang H, Kontos S, Ångström J, Cedervall J, Svedlindh P, Gunnarsson K and Sahlberga M 2016 *J. Solid State Chem.* **237** 300
[27] Mccurrie R, Rickman J, Dunk P and Hawkridge D 1978 *IEEE Trans. Magn.* **14** 682
[28] Breton J M L, Bran J, Folcke E, Lucis M, Lardé R, Jean M, Shieldb J E 2013 *J. Alloys Compd.* **581** 86
[29] Fazakas E, Varga L K and Mazaleyrat F 2007 *J. Alloys Compd.* **434** 611
[30] Zeng Q, Baker I, Cui J B and Yan Z C 2007 *J. Magn. Magn. Mater.* **308** 214
[31] Müllner P, Bürgler B E, Heinrich H, Sologubenko A S and Kostorz G 2002 *Philos. Mag. Lett.* **82** 71
[32] Zijlstra H and Haanstra H B 1966 *J. Appl. Phys.* **37** 2853
[33] Heusler F 1904 *Angew. Chem.* **17** 260
[34] Adams E 1952 *J. Appl. Phys.* **23** 1207
[35] Chen T and Stutius W 1974 *IEEE Trans. Magn.* **10** 581
[36] Guo X, Chen X, Altounian Z and Ström-Olsen J O 1992 *Phy. Rev. B* **46** 14578
[37] Yang J B, Kamaraju K, Yelon W B, James W J, Cai Q and Bollero A 2001 *Appl. Phys. Lett.* **79** 1846
[38] Yang J B, Yang Y B, Chen X G, Ma X B, Han J Z, Yang Y C, Guo S, Yan A R, Huang Q Z, Wu M M and Chen D F 2011 *Appl. Phys. Lett.* **99** 082505
[39] Ly V, Wu X, Smillie L, Shoji T, Kato A, Manabe A, Suzuki K 2014 *J. Alloys Compd.* **615** S285
[40] Poudyal N and Liu J P 2013 *J. Phys. D: Appl. Phys.* **46** 43001
[41] Cui J, Choi J P, Li G, Polikarpov E, Darsell J, Overman N, Olszta M, Schreiber D, Bowden M and Droubay T 2014 *J. Phys.: Condens. Matter* **26** 064212
[42] Yang J B, Yelon W B, James W J, Cai Q, Kornecki M, Roy S, Ali N and l'Heritier Ph 2002 *J. Phys.: Condens. Matter* **14** 6509
[43] Yoshida H, Shina T, Takahashi T and Fujimori H 1999 *Mater. Trans. JIM* **40** 455
[44] Liu Y, Zhang J, Cao S, Zhang X, Jia G, Ren Z, Li X, Jing C and Deng K 2005 *Phys. Rev. B* **72** 214410
[45] Ko K Y, Choi S J, Yoon S K and Kwon Y S 2007 *J. Magn. Magn. Mater.* **310** e887
[46] Zhang D T, Geng W T, Yue M, Liu W Q, Zhang J X, Sundararajan J A, Qiang Y 2012 *J. Magn. Magn. Mater.* **324** 1887
[47] Kirkeminde A, Shen J, Gong M, Cui J and Ren S 2015 *Chem. Mater.* **27** 4677
[48] Vuong Nguyen V, Poudyal N, Liu X B, Liu J P, Sun K, Kramer M J, Cui J 2014 *Mater. Res. Express* **1** 036108
[49] Rama Rao N V, Gabay A M, Li W F and Hadjipanayis G C 2013 *J. Phys. D: Appl. Phys.* **46** 265001
[50] Yang Y B, Wei J Z, Peng X L, Xia Y H, Chen X G, Wu R, Du H L, Han J Z, Wang C S, Yang Y C, Yang J B 2014 *J. Appl. Phys.* **115** 17A721
[51] Zhang D T, Geng W T, Yue M, Liu W Q, Lu Q M, Zhang J X, Guo Z H, Li W, Sundararajan J A, Qiang Y 2014 *J. Appl. Phys.* **115** 17A746
[52] Ma Y L, Liu X B, Gandha K and Vuong N V 2014 *J. Appl. Phys.* **115** 17A755
[53] Yang J B, Yelon W B, James W J, Cai Q, Roy S and Ali N 2002 *J. Appl. Phys.* **91** 7866
[54] Yang Y B, Chen X G, Wu R, Wei J Z, Ma X B, Han J Z, Du H L, Wang C S, Yang Y C, Zhang Y, Yang J B 2012 *J. Appl. Phys.* **111** 07E312
[55] Yang Y B, Chen X G, Guo S, Yan A R, Huang Q Z, Wu M M, Chen D F, Yang Y C, Yang J B 2013 *J. Magn. Magn. Mater.* **330** 106
[56] Kronmüller H, Yang J B and Goll D 2014 *J. Phys.: Condens. Matter* **26** 064210
[57] Zhou D, Zhang Y F, Ma X B, Liu S Q, Han J Z, Zhu M G, Wang C S and Yang J B 2015 *Chin. Phys. Lett.* **32** 127502
[58] Stoner E C and Wohlfarth E P 1948 *Phil. Trans. R. Soc. A* **240** 599
[59] Kronmüller H, Durst K D and Martinek G 1987 *J. Mag. Mag. Mater.* **69** 149
[60] Albert P A and Carr W J J 1961 *J. Appl. Phys.* **32** S201
[61] Kondorsky E 1940 *J. Phys.* **11** 161
[62] Schubert K, Meissner H G, and Rossteutscher W 1964 *Einige Strukturdaten Metallischer Phasen* (Berlin: Naturwissenschaften) **11** 287
[63] Meissner H G, Schubert K and Anantharaman T R 1965 *Proc. Indian Acad. Sci. Sect. A* **61** 340

[64] Huh Y, Kharel P, Shah V R, Li X Z, Skomski R and Sellmyer D J 2013 *J. Appl. Phys.* **114** 013906

[65] Rode K, Baadji N, Betto D, Lau Y C, Kurt H, Venkatesan M, Stamenov P, Sanvito S, Coey J M D, Fonda E, Otero E, Choueikani F, Ohresser P, Porcher F and André G 2013 *Phys. Rev. B Condens. Matter* **87** 184429

[66] Sakuma A 1998 *J. Magn. Magn. Mater.* **187** 105

[67] Zhu L and Zhao J 2013 *Appl. Phys. A* **111** 379

[68] Mix T, Müller K H, Schultz L and Woodcock T G 2015 *J. Magn. Magn. Mater.* **391** 89

[69] Lu Q M, Yue M, Zhang H G, Wang M L, Yu F, Huang Q Z, Ryan D H and Altounian Z 2015 *Sci. Rep.* **5** 17086

[70] Krén E and Kádár G 1970 *Solid State Commun.* **8** 1653

[71] Mizukami S, Kubota T, Wu F, Zhang X, Miyazaki T, Naganuma H, Oogane M, Sakuma A ando Y 2012 *Phys. Rev. B* **85** 014416

[72] Winterlik J, Balke B, Fecher G H, Felser C, Alves M C M and Bernardi F and.Morais J 2008 *Phys. Rev. B* **77** 054406

[73] Rode K, Baadji N, Betto D, Lau Y C, Kurt H, Venkatesan M, Stamenov P, Sanvito S, Coey J M D, Fonda E, Otero E, Choueikani F and Ohresser P 2013 *Phys. Rev. B* **87** 184429

[74] Zhao H, Yang W, Shao Z, Tian G, Zhou D, Du, H, Liu S, Han J, Wang C, Xu J, Yu D, Yang Y, Yang J 2017 *Scri. Mater.* **129** 6

[75] Wei J Z, Wu R, Yang Y B, Chen X G, Xia Y H, Yang Y C, Wang C S and Yang J B 2014 *J. Appl. Phys.* **115** 17A736

[76] Lu X S, Liang J K and Zhou M G 1980 *Acta Phys. Sin.* **29** 469 (in Chinese)

[77] Wachtel E and Nier K J 1965 *Z. Metallk* **56** 779

[78] Okamoto H 2010 *Desk Handbook: Phase Diagrams For Binary Alloys* (2nd Edn.) (ASM International Materials Park, Ohio 44073-0002) p. 400

[79] Kazuhiro Minakuchi, Umetsu Y, Kiyohito Ishida, Ryosuke Kainuma 2012 *J. Alloys Compd.* **537** 332

[80] Kurt H, Rode K, Venkatesan M, Stamenov P and Coey J M D 2011 *Phys. Rev. B* **83** 020405(R)